CHAPTER V
RESULTS AND DISCUSSION

5.1 Synthesis of Carbon nanoparticles

5.1.1 Temperature profile of the tubular quartz reactor

Since a tubular reactor is employed for pyrolysis of ferrocene and glycerol mixture the temperature distribution along the axial direction of the reactor is a crucial parameter to be known before conducting other experiments. The temperature profile has been determined by inserting the thermocouple into the tube then moving its tip with a step size of 2 centimeters after achieving the set point of 900 °C. The temperature distribution has been shown in figure 5.1. The curve exhibits a symmetric distribution and a maximum value is at the middle of the tube. In practice, the mixture of ferrocene and glycerol contained in an alumina boat was placed at the position of which temperature is higher than 300°C (14 cm. from inlet) in the experiment because it is the condition that the mixture could be vaporized without decomposition.

Pyrolysis process has been started by vaporization of the mixture and nitrogen gas as a carrier gas will carry the vapors to the downstream zone where the decomposition could take place. After the operating time of 30 minutes, the obtained product is collected by sweeping from the inner tube wall. The products have been characterized by electron microscopy, EDX, XRD, DLS with zeta potential analysis and BET analysis.

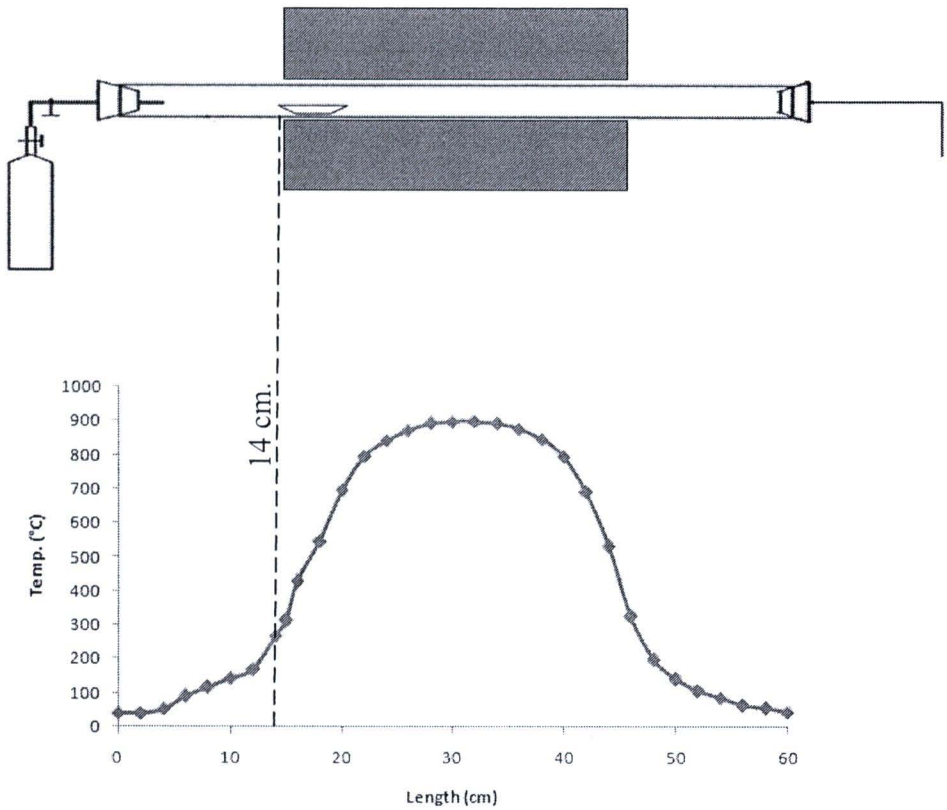

Figure 5.1 Temperature distribution of the reactor

5.1.2 Microscopic analysis

5.1.2.1 SEM and TEM analysis

As the product from co-pyrolysis process, a black film fully coved the inner surface of the tubular quartz reactor wall. The synthesized products were swept from the inner wall surface for SEM and TEM analysis.

Bases on typical SEM observation, the as-grown product consists of large amount of entangling carbon nanotubes (CNTs) with a few spherical carbon nanoparticles as shown in figure 5.2. The obtained product is CNTs with diameters of 40 to 80 nm with length of several microns. However, some agglomerations of very fine particles also deposit on the tube tube bundle surface. On the top edge of the tube bundles, there are many fine particles with different morphology as shown in figure 5.3. It would be able to verify later that those particles are iron clusters encapsulated in carbon shell.

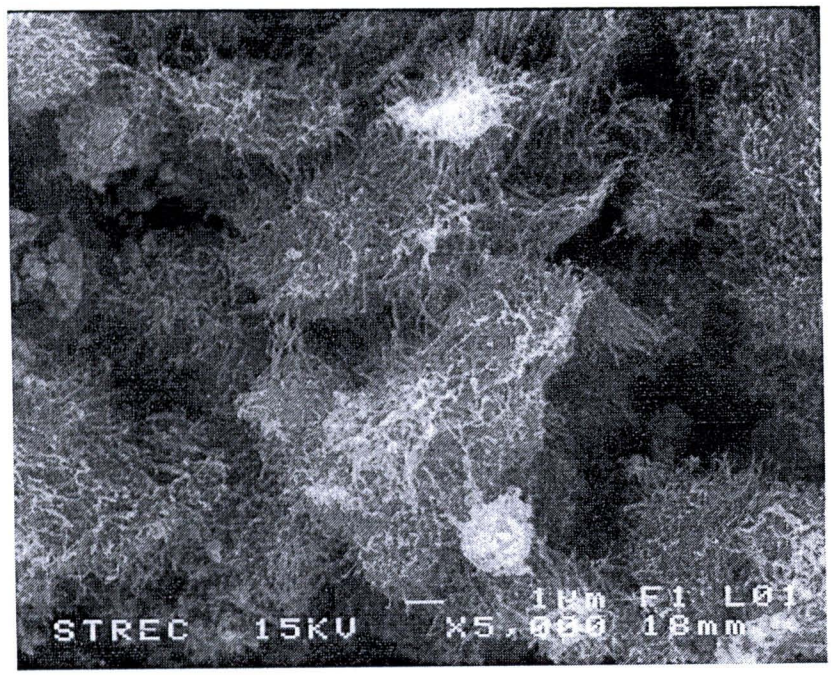

Figure 5.2 SEM images of the synthesized products

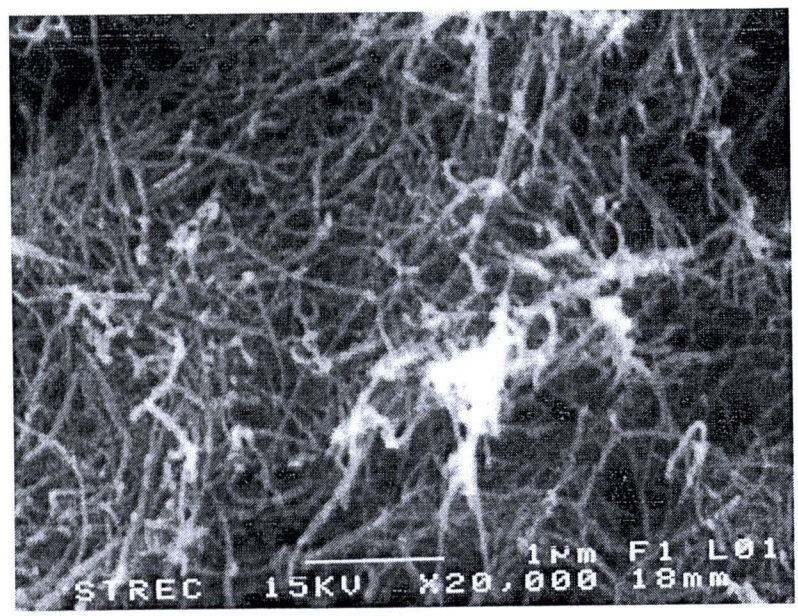

Figure 5.3 Higher magnification of SEM images of the synthesized products

For further investigation of the morphology of the synthesized products, a carefully sampled product is dispersed in toluene and ultrasonicated before dropped on a copper grid for TEM observation. As shown in figure 5.4, the low magnification of the TEM image of the obtained product illustrates that most of the obtained particles are CNTs with diameters of 40-80 nm and carbon nanocapsules (CNCs). Moreover, the obtained products are multi-walled carbon nanotubes (MWCNTs) with iron particles filled in the tubes and at the tube tip and multi-shell carbon nanocapsules with iron particles which were encapsulated in the core. These results are in good agreement with the SEM observation that the as-grown product consists of large amount of entangling carbon nanotubes.

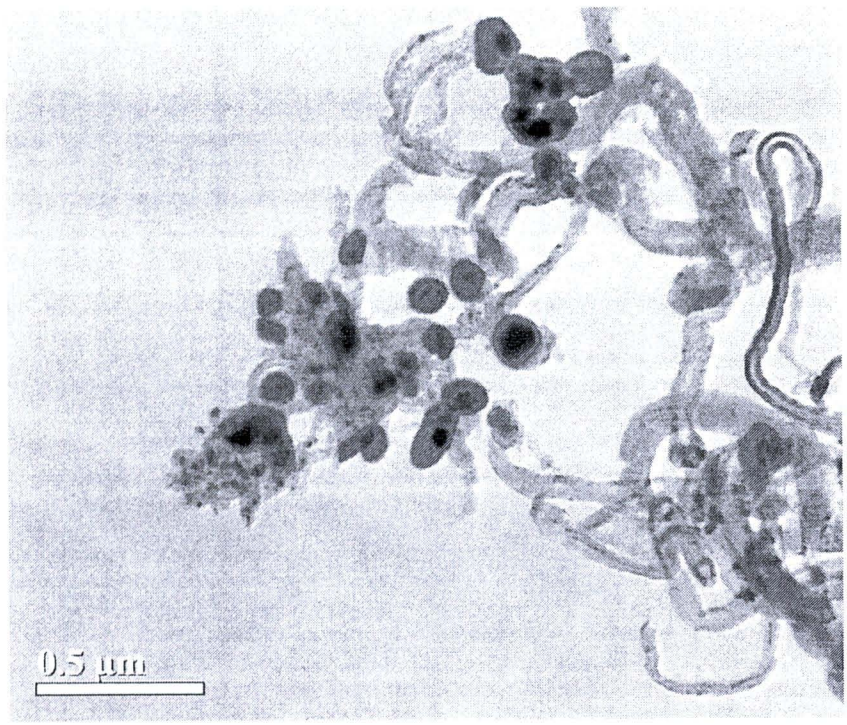

Figure 5.4 The low magnification of the TEM image

Higher magnification of TEM images of CNPs obtained also reveals that the obtained nanotubes are multi-walled carbon nanotubes (MWCNTs) and the obtained spherical carbon nanoparticles are multi-shell carbon nanocapsules as shown in figure 5.5. It suggests that these products are obtained from the growth of carbon atoms induced by iron clusters. As also prepared by Charinpanitkul et al. (2009) and Sano et al. (2004), formation of carbon shell would take place after the condensation of Fe clusters emitted from the decomposition of ferrocene [2, 7]. Because of the presence of Fe clusters within the internal structure of these carbon nanoparticles, our synthesized products exhibit a good respond to magnetic field.

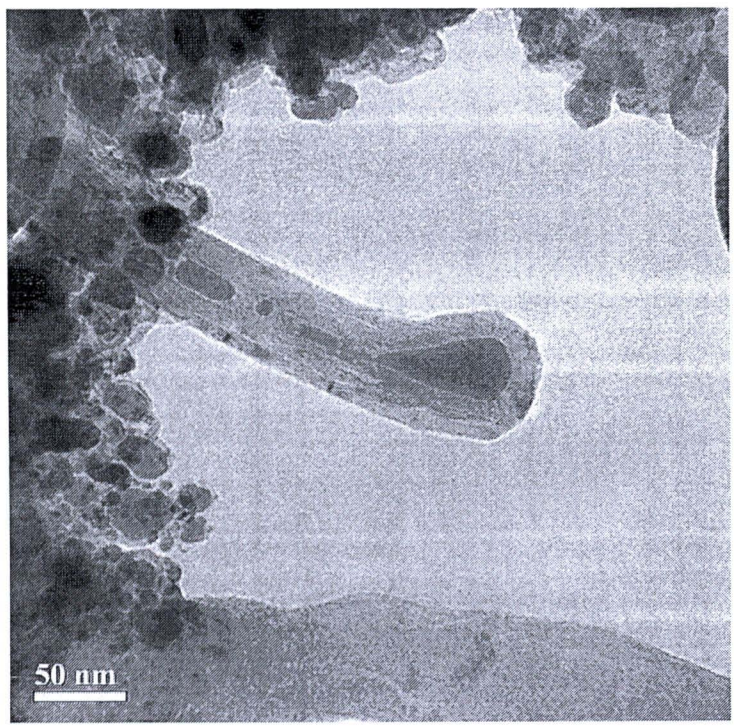

Figure 5.5 Higher magnification of the TEM image

5.1.2.2 Elemental analysis

5.1.2.2.1 Energy dispersive X-ray (EDX)

The energy dispersive X-ray (EDX) spectroscopic analysis has been performed for elemental analysis as shown in figure 5.6. From the result, it is found that the obtained products were composed mainly of carbon (77.34 wt %) and Fe (14.32 wt %). This confirms that iron particles exist in the synthesized products. Further investigation on the phase and crystalline structure of these Fe clusters would be conducted by XRD analyzer and discussed later in 5.1.2.2.2.

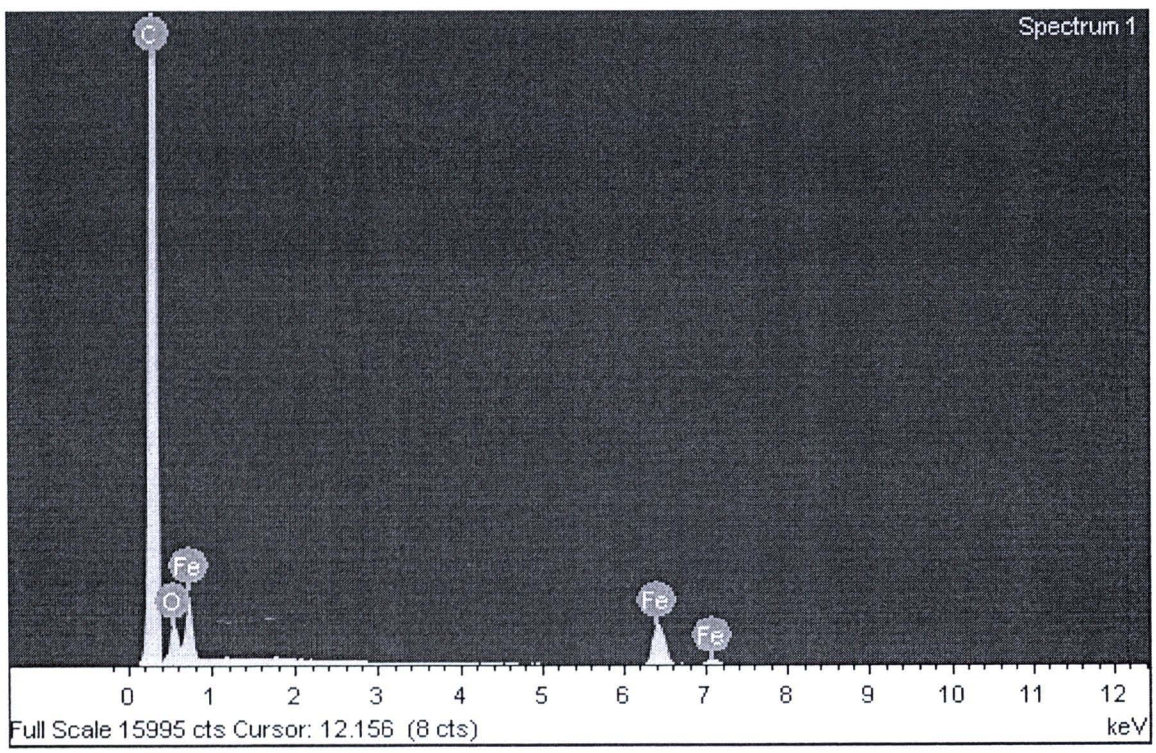

Figure 5.6 EDX spectrum of CNTs from co-pyrolysis at 900 °C

5.1.2.2.2 X-ray Diffraction (XRD) analysis

XRD characterization is performed to further validate the corresponding structure of the core and shell of nanoparticles. The XRD result of the as-synthesized products from ferrocene-glycerol mixture with molar ratio of 5:1 at 900□C is shown in figure 5.7. The diffraction peak at about 26.3□can be assigned to the (002) planes of hexagonal graphite structure. The iron cores are crystalline and exhibit the (110) plane of the fcc-Fe crystal (face-centered cubic) at XRD peak 43.7□ In addition, it can be seen the others peak from the result such as: bcc-Fe (110) at 44.7□, fcc-Fe (200) at 48.8□ However, it can observe iron carbide (Fe_3C) and iron oxide (Fe_2O_3) with including in the as-grown prepared CNPs.

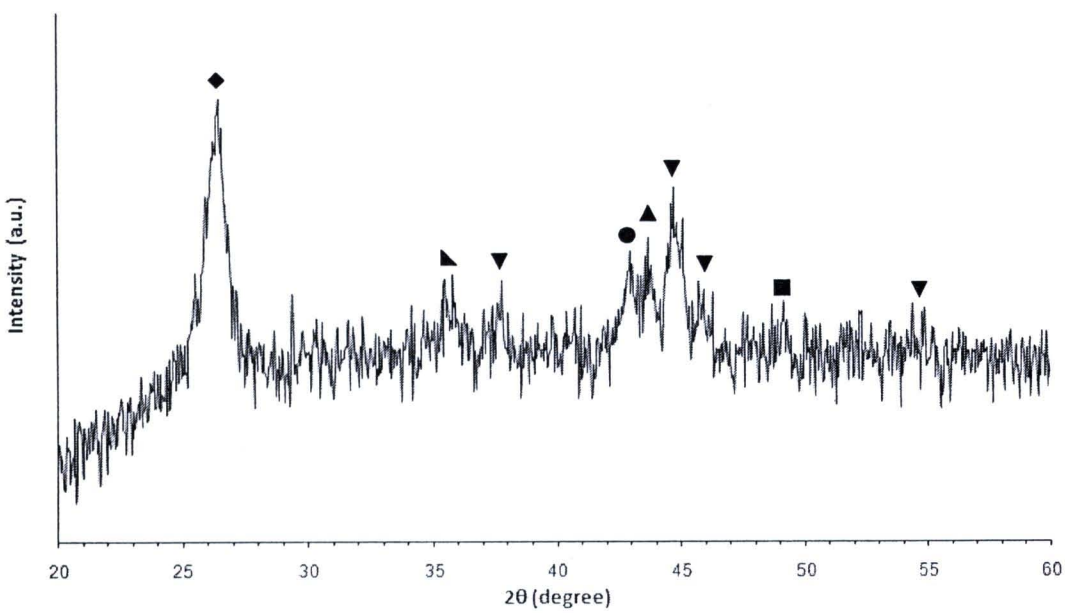

Figure 5.7 XRD pattern of products obtained at 900□C with molar ratio of 1:5

◆ (002) Graphite structure (26.3□) ▲ (110) bcc-Fe (44.7□)

● (111) fcc Fe (43.7□) ▼ Fe_3C (iron carbide)

■ (200) fcc-Fe (48.8□) ◣ Fe_2O_3

It should be noted that the iron particles in the as-grown products are in the form of iron oxide (Fe_2O_3), which is obtained by a reaction of oxygen remained in the process from glycerol, and in the phase of iron carbide (Fe_3C) and metallic phase of bcc-Fe (110) fcc-Fe (111) and fcc-Fe (200). The well-crystallized graphite could be recognized as higher diffraction peak.

5.1.2.2.3 Dynamic Light Scattering (DLS) with zeta potential

Dynamic Light Scattering characterization is performed to determining particle size distribution and zeta potential of the synthesized CNPs. The as-grown film of CNPs is sampled and dispersed in toluene and then ultrasonicated for 15 minutes. A typical well dispersed sample is characterized for their particle size distribution by ZETASIZER 300HSA as which is shown in figure 5.8.

Based on experimental results, the hydrodynamic diameter of the obtained CNPs is in a range of 105-1200 nm which higher than SEM observation due to the agglomeration of the obtained CNPs.

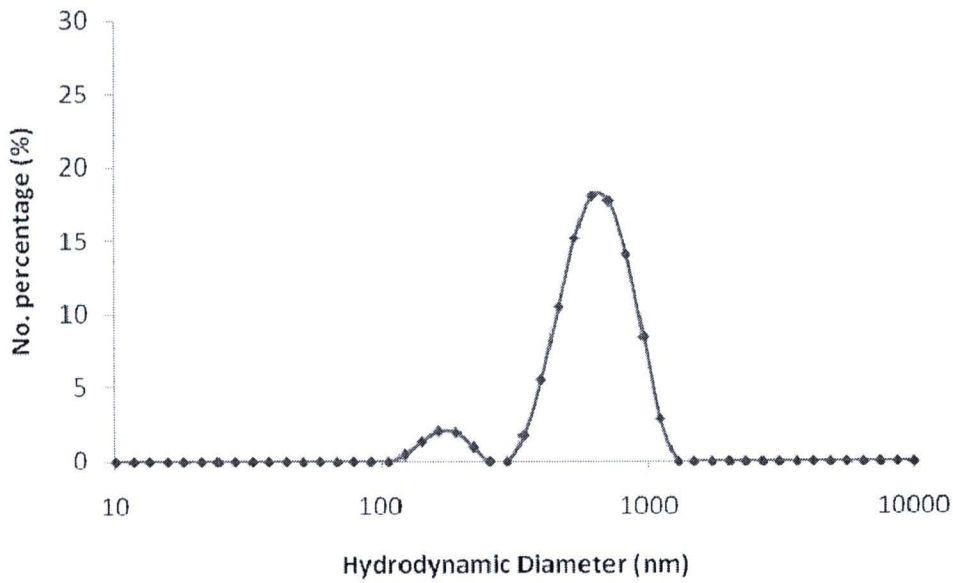

Figure 5.8 Particle size distributions of CNPs obtained from co-pyrolysis of Ferrocene and Glycerol with molar ratio of 1: 5 at 900 °C.

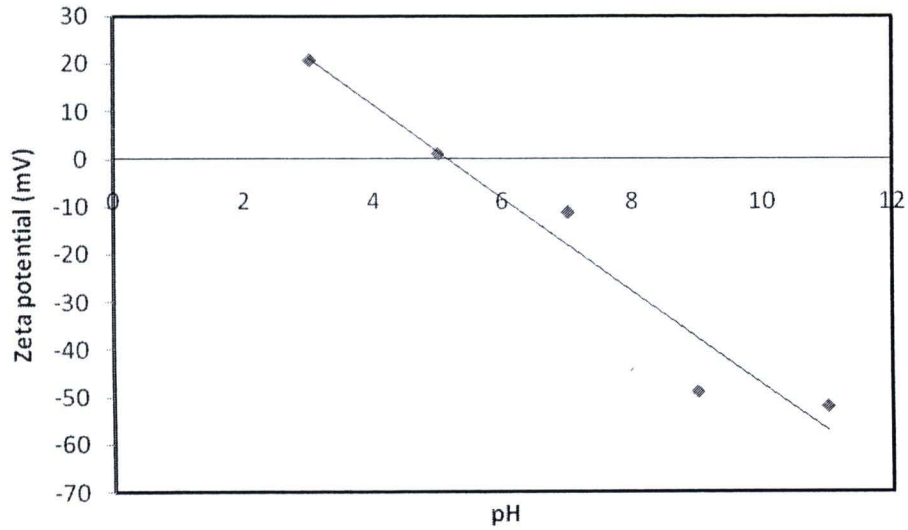

Figure 5.9 zeta potential of the CNPs.

The as-grown CNPs is also characterized for zeta potential as shown in figure 5.9. From the zeta potential result, it is indicated that the surface of CNPs was positively charged when solution pH was below 5.1 and negatively charge when solution pH was above 5.1. Therefore, it should be note that the pH of the zero point of charge (pH_{zpc}) for the obtained CNPs was determined to be 5.1 which similar with the results of Wu [17] and Kuo et al. [18].

5.1.3 Porosity analysis

The porosity of synthesized CNPs was determined by adsorption-desorption of nitrogen gas at 77 K using a BET analyzer (*BEL: BELSORP-mini, Japan*). Typical isotherms of adsorption-desorption of synthesized CNPs was demonstrated in Figure 5.10. From the result, the isotherm of synthesized CNPs can be classified as a type IV isotherm, according to the International Union of Pure and Applied Chemistry (IUPAC) nomenclature [23] which indicated the existence of micropore and mesopore structure. Specific BET surface area (S_{BET}), total pore volume (V_{tot}), mesopore volume (V_{mes}) and average pore diameter (D_{avg}) are presented in table 5.1. The pore size distribution data calculated (as shown in figure 5.11) from the adsorption branches of nitrogen isotherms by the BJH (Barrett-Joyner-Halenda) method showed that the synthesized CNPs exhibit a modal pore size radius of 3.76 nm with a noticeable pore size radius distribution smaller than 100 nm.

Table 5.1 Porosity analysis of synthesized CNPs

N_2 adsorption-desorption at 77 K	
S_{BET} [m^2/g]	73.851
V_{tot} [cm^3/g]	0.2668
V_{mes} [cm^3/g]	0.2559
D_{avg} [nm]	18.453
D_p [nm]	7.52

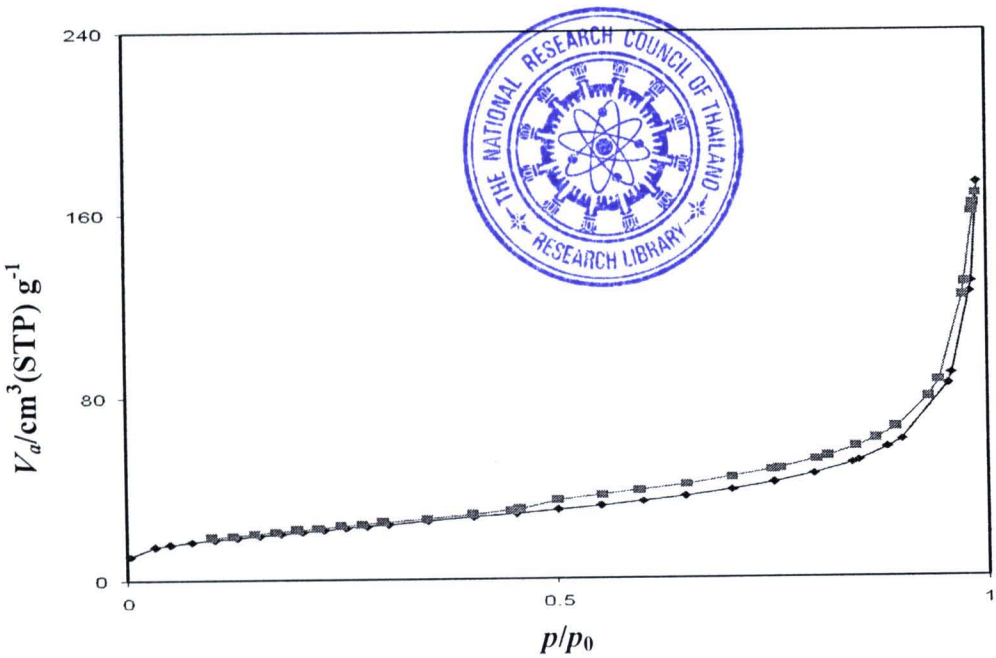

Figure 5.10 N_2 adsorption-desorption isotherm of synthesized CNPs (■) Adsorption and (●) Desorption

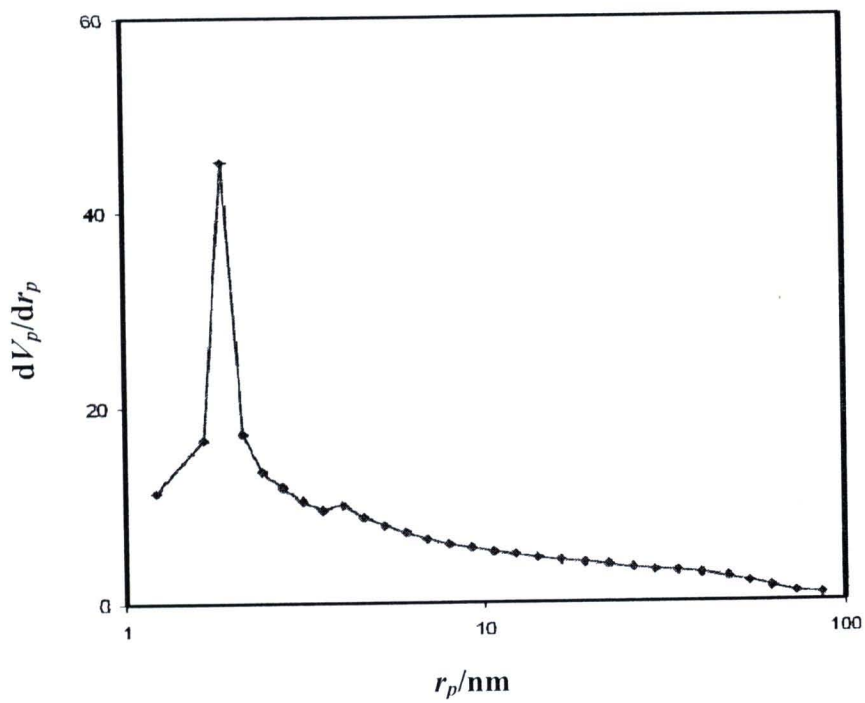

Figure 5.11 The pore size radius distribution

5.2 Effect of operating variables on dye adsorption performance

In this study, the adsorption efficiencies are investigated. Aqueous solution of Methylene Blue (C.I. Basic Blue 9, MB), Benefix Black B (C.I. Reactive Black 5, B5) and Benecion Red H8B (C.I. Reactive Red 31, R31) are used for all adsorption experiment. All batch adsorption experiments were analyzed with a UV-vis spectrophotometer (UV-1700PC, Japan) at appropriate wavelength corresponding to the maximum absorbance (λ_{max}) of 664, 595 and 540 nm for MB, B5 and R31, respectively. The amount of dye adsorbed per unit mass adsorbent was calculated by the equation 5.1.

$$Q_t = \frac{C_0 - C_t}{W} V \qquad (5.1)$$

Where Q_t (mg/g) is the amount of dye adsorbed per unit mass adsorbent at any time t, C_0 (mg/L) is the initial dye concentration, C_t (mg/L) is the dye concentration at any time t(min), V (L) is the volume of solution and W (g) is the weight of the CNPs.

If adsorption is reversible and the adsorption and desorption rates equal each other for the system to be steady state. In this case, the steady state, which are assumed that is a well-mixed condition by the concentration profile, is also an equilibrium state because there are no net molecular fluxes. Therefore, Q_e (mg/g) and C_e (mg/l) are the amount of equilibrium dye adsorbed per unit mass adsorbent and the equilibrium dye concentration [30]. The united state environmental protection agency also suggested that the equilibrium state should be the time needed to establish a rate of change of the solute concentration in solution equal to or less than 5% per a day. [31].

5.2.1 Effect of contact time

Figure 5.12 presents the adsorption performance on CNPs as function of contact time. The effect of contact time on the removal of MB, B5 and R31 with the initial concentration of 40 mg/L, initial pH value of 6 and quantity of initial CNP adsorbents of 0.5 g/L are carried out. As explaining in 4.4, suspension of synthesized CNPs in solution of each dye solution was subject to ultrasonicated for 10 minutes.

Immediately after sonication, 10 ml of solution was sampled for detecting the amount of remaining dye.

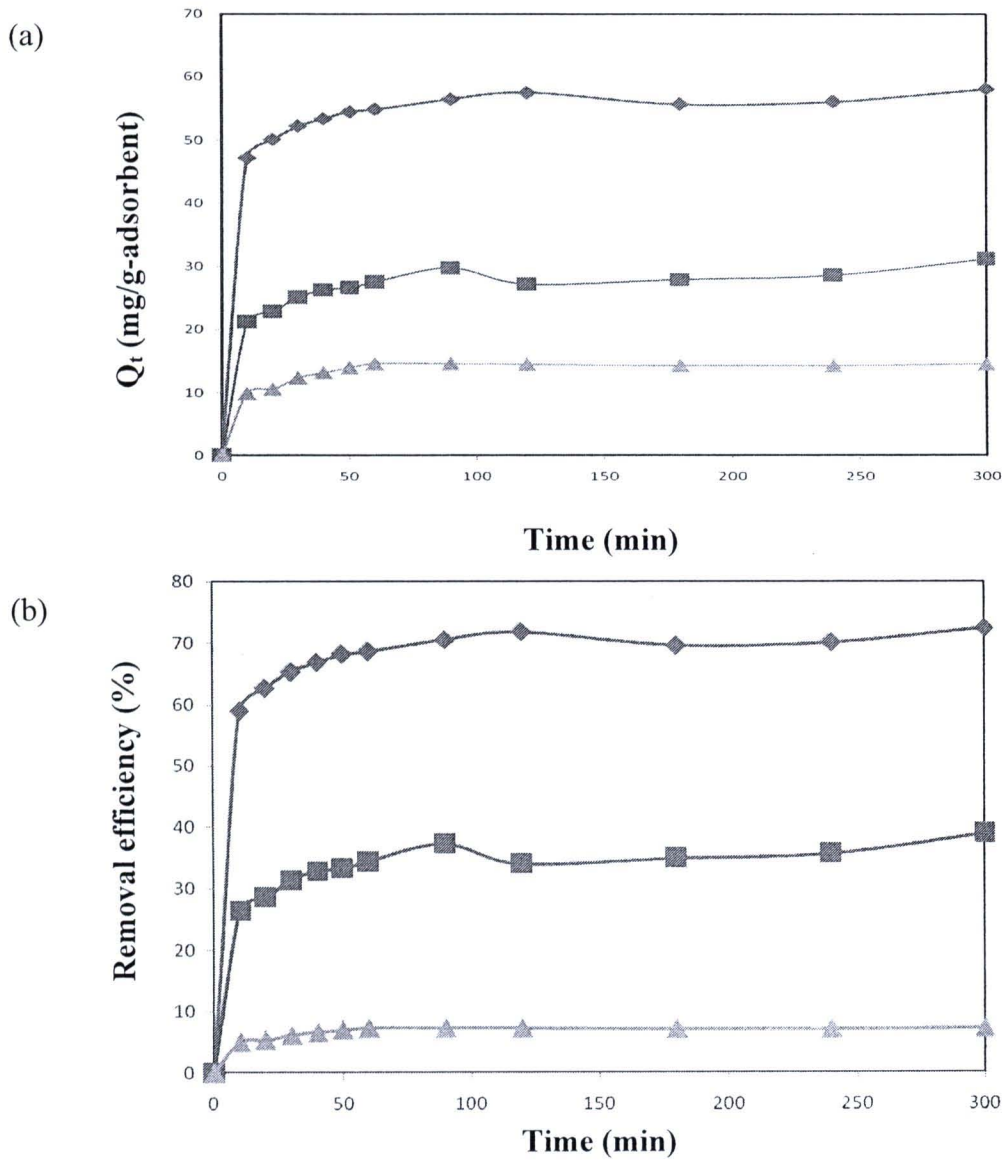

Figure 5.12 Plots of (a) amount of dye adsorbed and (b) removal efficiency of (▲)MB, (♦)B5 and (■)R31 as a function of time

A rapid uptake of the dye adsorbed by synthesized CNPs occurred within a short time period followed by a slower stage until 60 minutes. After 60 min, no significant concentration change was found. Regardless of dye type, a rapid decrease in the concentration of dye remaining in the solution could be observed. It would be

reasonable to imply that all results represent a consistent trend of dye removal with respect to contact time. Similar observations could be found in literature. Luo et al. [26], who utilized halloysite nanotubes to adsorb Neutral Red (NR), suggested that the amount of NR adsorbed increased with the increase in contact time and reach the equilibrium within 30 minutes. Similar results were also obtained for adsorption MB and NR onto MWCNTs filled with Fe_2O_3 particles by Qu et al. [15] and for removal Brilliant Green onto carbon/iron oxide nanocomposite Ahmad and Kumar [27]. In addition, based on these results, further investigation would be conducted with respect to a constant contact time of 300 min.

5.2.2 Effect of initial dye concentration

The effect of initial dye concentration was inestigated in the range of 10 to 100 mg/L and 0.5 g/L CNPs loading at 25 °C for 6 hours. Figure 5.13 show plot of the removal efficiency versus initial dye concentration.

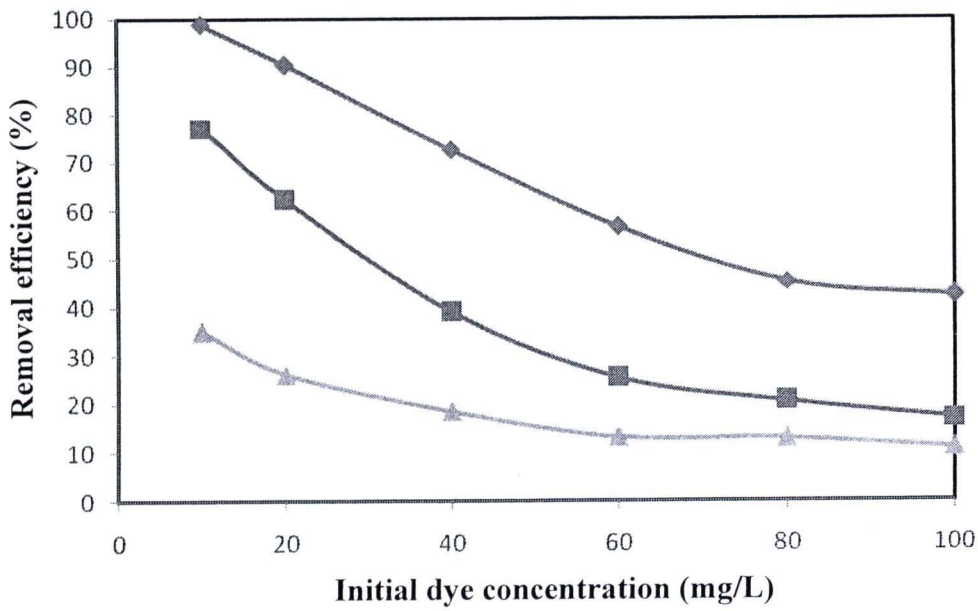

Figure 5.13 Plots of removal efficiency versus initial dye concentration: (▲)MB, (♦)B5 and (■)R31

When the initial concentration increased from 10 to 100 mg/L, the removal efficiency decreased from 98.77 % to 42.47 %, 77.13 % to 17.13 % and 34.99 % to 11.05 % for B5, R31 and MB, respectively. The similar results can be observed by Amin [28], Therani-Banga et al. [33] and Shu [34]. Base on these result, it would be reasonable to imply that the initial dye concentration is one of an important factor in adsorption capacity of MB, B5 and R31 on synthesized CNPs.

5.2.3 Effect of the amount of CNPs loading

The amount of adsorbent loading is an important parameter in the determination of adsorption capacity. The effect of the amount of CNPs loading was investigated in the range from 0.3 g/L to 0.9 g/L with a constant of initial dye concentration of 60 mg/L and initial pH value of 6.

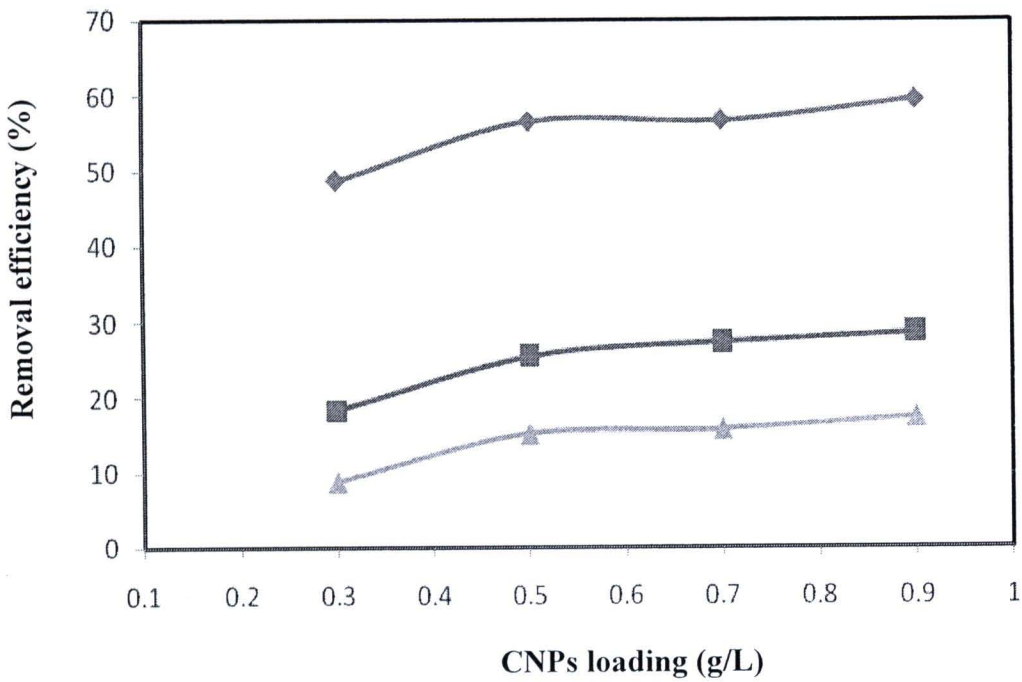

Figure 5.14 Plots of removal efficiency versus the amount of CNPs adsorbent: (▲)MB, (♦)B5 and (■)R31

Figure 5.14 presents the removal efficiency increased with increasing of the dose of CNPs. However, they were not significantly altered beyond CNPs loading of 0.5 g/L. From the result, it suggested that increasing the CNPs dose increases the available active site on surface, leading to increase the adsorption on the available adsorbent surface. However, increasing of CNPs loading might increase the probability of the entanglement and agglomeration of CNPs, leading to decrease the adsorption on the overlapped external surface. The similar results can be observed by Amin [28], who utilized activated carbon from sugarcane bagasse pith to removal reactive dye in aqueous solution. The similar result was also obtained from Kuo et al. [18] and Luo et al. [26]. Based on these results, further investigation would be conducted with respect to a constant CNPs loading of 0.5 g/L.

5.2.4 Effect of initial pH value

The effect of initial pH value on adsorption efficiency experiments were studied over a range from 3 to 11 (±0.2). The experiments were carried out with initial dye concentration of 100 mg/L and 0.5 mg/L adsorbent. The results are shown in figure 5.15. It was observed that B5 and R31 removal efficiency decreased when pH value increased. The result may be explained by the electrostatic attraction between charged surface of CNPs and dyes.

As the zeta potential result in figure 5.9, when solution pH decreased, enhancing the electrostatic attraction between negative charged dye anions and positively charged surface of CNTs. Therefore, the removal efficiency of B5 and R31 was relatively high when the solution pH was below pH_{zpc}.

On the other hand, MB adsorbed is not significantly altered. MB is basic dye which can be classified as cationic dyes. It was observed that MB adsorbed increased with increasing pH value from 3 to 5 and then decreased slightly with further increasing pH value from 5 to 7. With further increasing pH value, MB adsorbed is not significantly changed. In pH range of 7 to 11, MB removal are higher than pH of 3, it might be from increasing the number of electrostatic attraction between the positively charged cationic dyes and negatively charged CNPs sites.

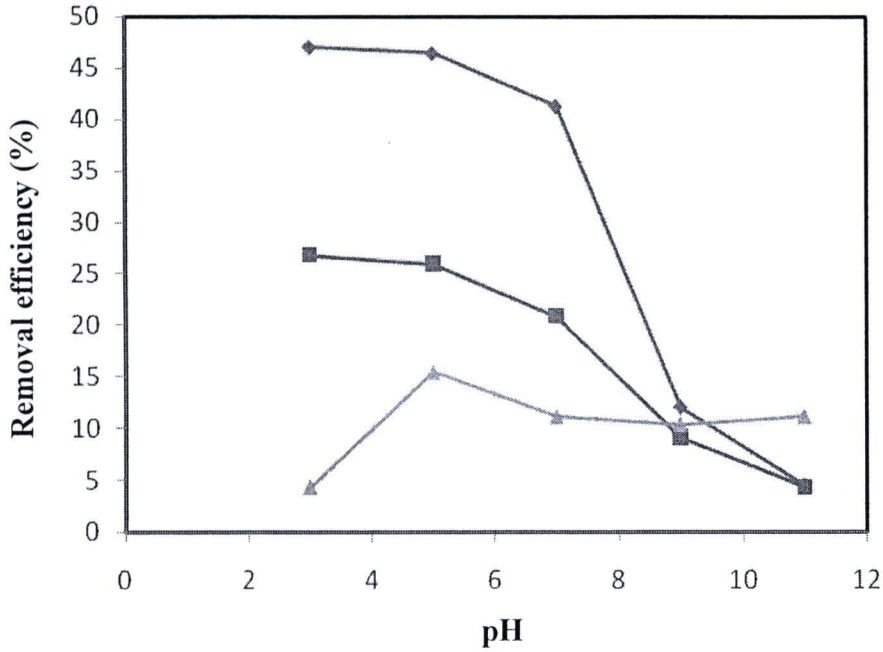

Figure 5.15 Effect of initial pH value of the solution on the adsorption of (▲)MB, (♦)B5 and (■)R31 (C_0=100 mg/L, 0.5 g/L CNPs and contact time = 5 h.)

5.3 Adsorption isotherm

On the adsorption experiment, the adsorption isotherms for Methylene blue (MB), Reactive B5 and Reactive Red31 at a constant temperature of 25 (± 2) °C was displayed in figure 5.16, which plot the relationships between the amount of dye adsorbed per unit mass adsorbent (Q_e) and the equilibrium concentration (C_e). The maximum adsorption capacities are 22.11, 34.26 and 84.94 mg/g for MB, R31 and B5, respectively. The experiment data were also analyzed with Langmuir and Freundlich isotherm models.

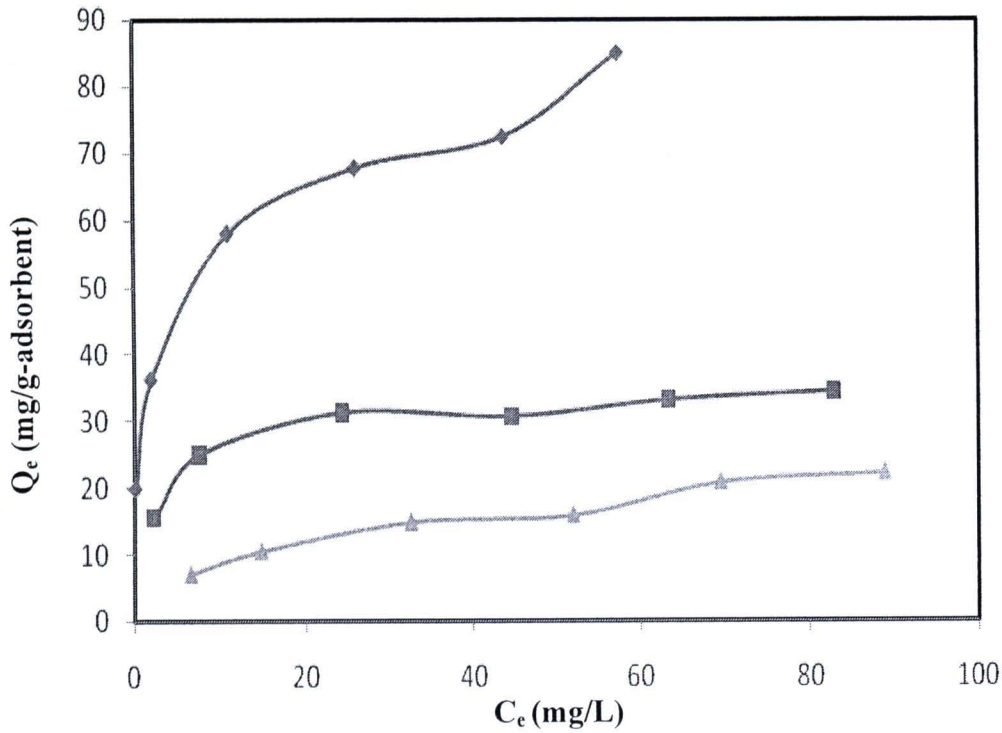

Figure 5.16 Adsorption isotherm of different typical dye at 25 °C:
(▲)MB, (♦)B5 and (■)R31

From the results, the sharp knee and the isotherm curve for B5, R31 and MB dyes indicates that the adsorption is favorable. In order to confirm the adsorption mechanism, Langmuir and Freundlich isotherms were used to describe the mechanism of the dye adsorption on CNPs.

The Langmuir isotherm model (From Eq.3.1 and 3.2) was chosen for estimation of the maximum adsorption capacity corresponding to complete monolayer coverage on the adsorbent surface. The adsorption isotherm of typical dyes on CNPs at 25 (± 2) °C, which revealed the relationship between C_e/Q_e and C_e was fitted with the data of Langmuir model as shown in figure 5.17.

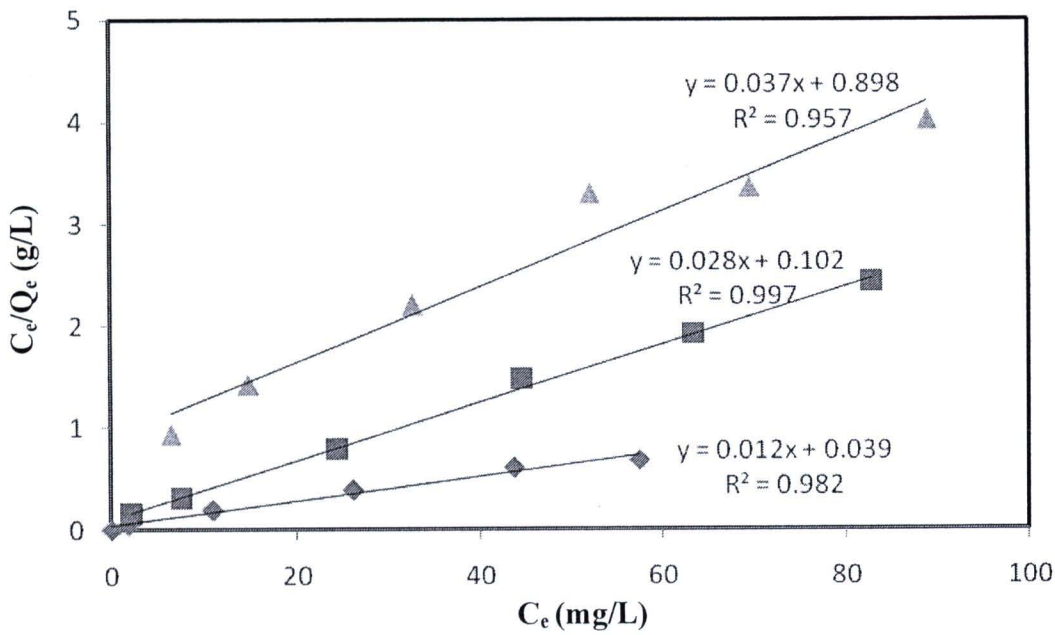

Figure 5.17 Langmuir plots for the adsorption of typical dye at 25 °C: (▲)MB, (♦)B5 and (■)R31

The Freundlich isotherm model (From Eq.3.3 and 3.4) was also chosen for describe the dye adsorption mechanism. Figure 5.18 displays the adsorption isotherm was fitted with the data of Freundlich model.

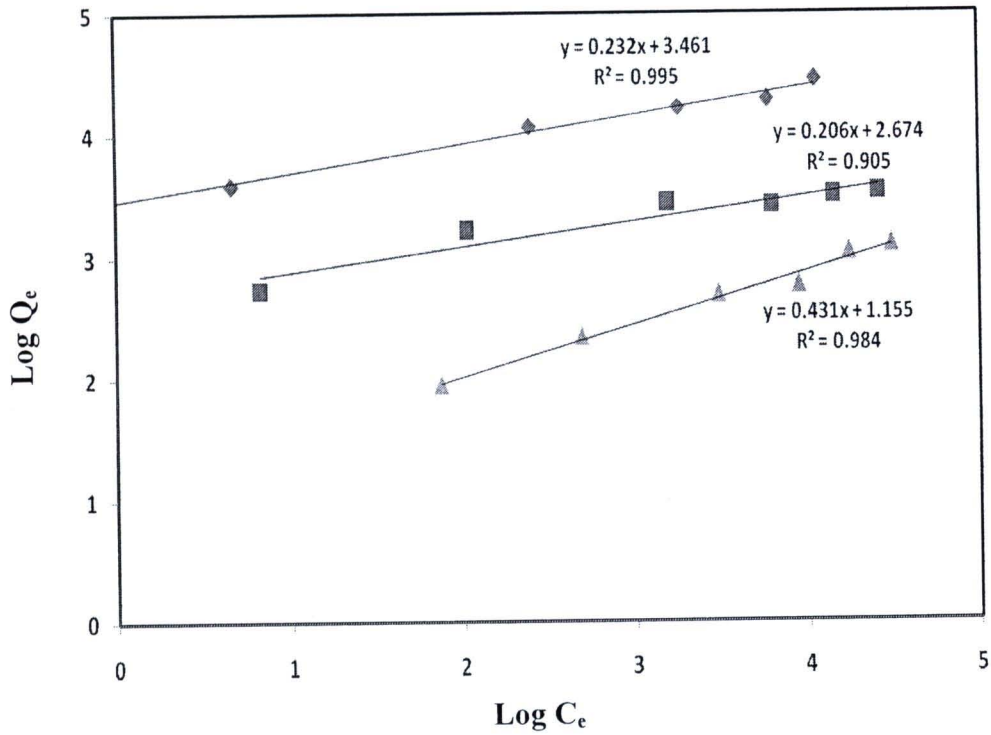

Figure 5.18 Freundlich plots for the adsorption of typical dye at 25 °C: (▲)MB, (♦)B5 and (■)R31

Table 5.2 Constant values of Langmuir and Freundlich isotherms for dye adsorption onto CNPs at 25 °C

Dye	Langmuir				Freundlich		
	Q_m (mg/g)	K_L (L/mg)	R_L	r^2	K_F (mg/g(mg/L)$^{1/n}$)	1/n	r^2
B5	83.333	0.308	0.0315-0.245	0.982	31.842	0.232	0.995
R31	35.714	0.275	0.035-0.267	0.997	14.488	0.206	0.905
MB	27.027	0.041	0.195-0.708	0.957	3.177	0.431	0.984

Table 5.2 summarized the coefficients of the Langmuir and Freundlich isotherms at 25 °C. Most of the r^2 values exceed 0.9. Based on the correlation coefficients (r^2), the experiment data of B5 and MB well fitted with Freundlich model and the experiment data of R31 well correlated with the Langmuir model. The lower Langmuir and Freundlich constant value (K_L and K_F) of the MB shows the weaker attraction toward the site of CNPs charge. K_L and K_F also indicates that the adsorption rate constant to desorption rate constant.

R_L lied between zero and unity, suggesting that the sorption is favorable for B5, R31 and MB on CNPs. The R_L values indicate that sorption is more favorable for the higher initial concentrations than for the lower ones. The sorption is very favorable for B5 and R31 and favorable MB. According to this classification, system favor ability tends to be in the order of B5 > R31 > MB.

Jiang et al. suggested that if $1/n$ less than unity, then the adsorption is physical; otherwise, the adsorption is chemical [29]. All values of $1/n$ less than 0.45, it would be reasonable to imply that the adsorption of three typical dyes in this study on synthesized CNPs is physical.

5.4 Kinetic model

In order to examine the mechanism and rate-controlling step, three kinetic models, pseudo first-order, pseudo second-order and intraparticle diffusion, are adopted to investigate the adsorption process with condition of initial dye concentration of 40 mg/l, CNPs loading of 0.5 g/L and initial pH value of 6.

Pseudo first-order equation:

$$\frac{dQ_e}{dt} = k_1(Q_e - Q_t) \tag{5.2}$$

From above equation, integrating it for the boundary condition t = 0 to t = t and Qt = 0 to Qt = Qt, it may be rearranged for linearized data plotting as shown below:

$$\ln(Q_e - Q_t) = \ln(Q_e) - k_1 t \tag{5.3}$$

where Q_e and Q_t are the adsorption capacity at equilibrium and time t(min), respectively, and k_1 (min^{-1}) is the rate constant of the pseudo first-order

Pseudo second-order equation:

$$\frac{dQ_e}{dt} = k_2(Q_e - Q_t)^2 \tag{5.4}$$

Integrating this for the boundary conditions t = 0 to t = t and Qt =0 to Qt = Qt, which is the integrated rate law for a pseudo second-order model and can be rearranged to obtain:

$$\frac{t}{Q_t} = \frac{1}{k_2 Q_e^2} + \frac{1}{Q_e} t \tag{5.5}$$

where k_2 (g/mg.min) is the second-order rate constant. The initial adsorption rate h (mg/g min) can be determined from $h=k_2 q_e^2$.

Intraparticle diffusion equation: $Q_t=k_pt^{1/2}+C$

where k_p (mg/g.min$^{1/2}$) is the intraparticle diffusion rate constant.

Table 5.3 Coefficients of pseudo first-order kinetic model

Dye	Pseudo first-order			
	$Q_{e,exp}$ (mg/g)	$Q_{e,cal}$ (mg/g)	K_1 (min^{-1})	r^2
B5	58.020	5.883	0.007	0.414
R31	31.154	6.303	0.004	0.393
MB	14.567	1.590	0.022	0.277

Table 5.4 Coefficients of pseudo second-order kinetic model

Dye	Pseudo second-order				
	$Q_{e,exp}$ (mg/g)	$Q_{e,cal}$ (mg/g)	K_2 (g/mg.min)	h (mg/g min)	r^2
B5	58.020	58.824	0.0056	19.231	0.999
R31	31.154	31.250	0.0042	4.115	0.995
MB	14.567	14.925	0.0162	3.610	0.999

Table 5.5 Coefficients of intraparticle diffusion model

Dye	Intraparticle diffusion	
	K_p (mg/g.min$^{1/2}$)	r^2
B5	1.458	0.946
R31	1.360	0.981
MB	0.843	0.896

From the results, the pseudo first-order is not well fitted for B5, R31 and MB. Moreover, all of the calculated values of $Qe_{,cal}$ (mg/g) are far from the experimental values $Qe_{,exp}$ (mg/g). So the psuedo first-order kinetic model is not suitable to discribe the adsorption process as shown in figure 5.19.

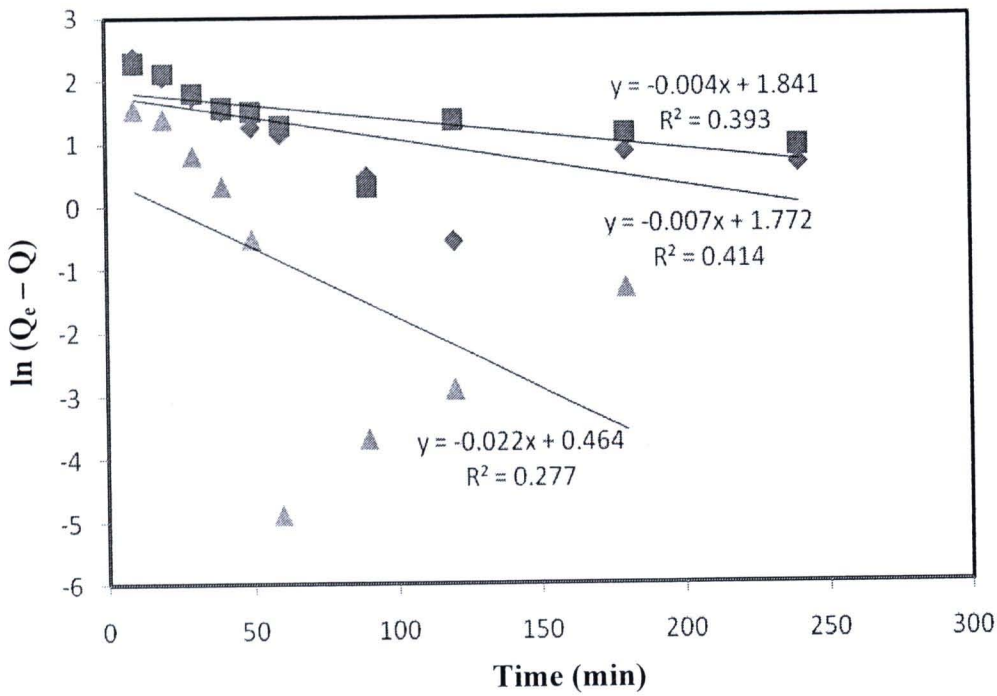

Figure 5.19 Regression of pseudo first-order model of (▲)MB, (♦)B5 and (■)R31:

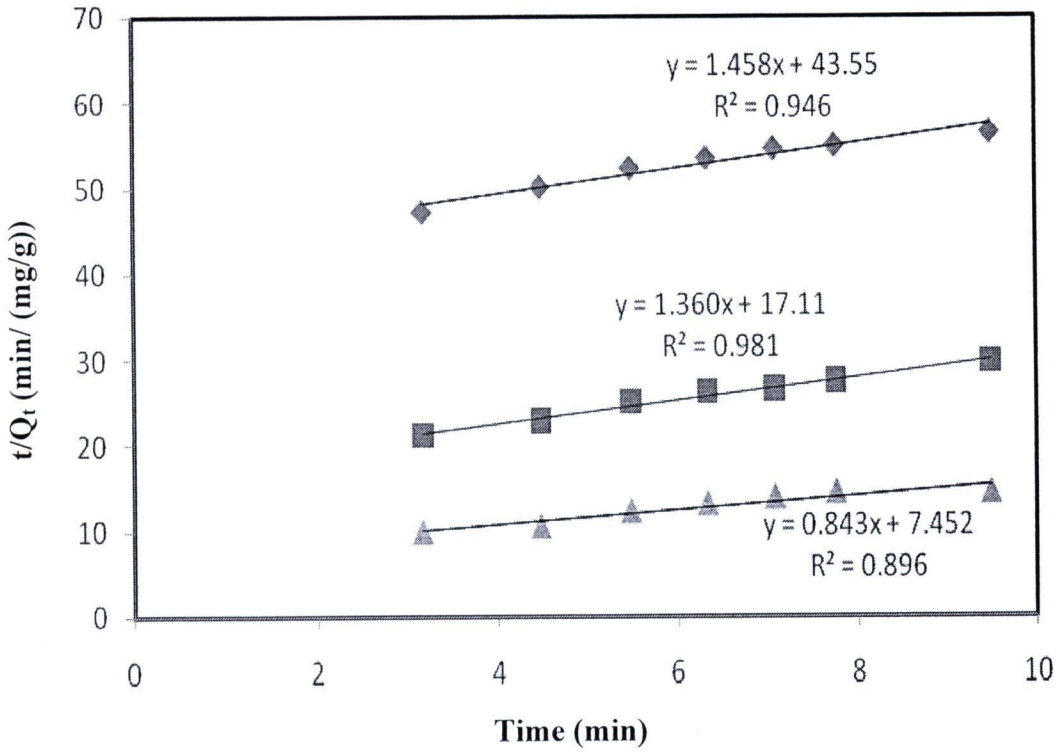

Figure 5.20 Regression of pseudo second-order model of (▲)MB, (♦)B5 and (■)R31

However, regression of pseudo second-order was linear with the correlation coefficients (r^2) higher than 0.99. Furthermore, the calculated values of $Qe_{,cal}$ (mg/g) was consistent with the experimental values $Qe_{,exp}$ (mg/g). This study indicated that the psuedo second-order model can describe the adsorption process well as shown in figure 5.20.

Generally, the adsorption process on porous adsorbents has four steps. First step is external diffusion. The second step is film diffusion. The third is intra particle diffusion and the last step is finally adsorption of the solute onto the surface. Because neither the pseudo first-order nor pseudo second-order model can identify the diffusion mechanism during the adsorption process, the experimental data were analyzed by the intraparticle diffusion model for explain the diffusion mechanism.

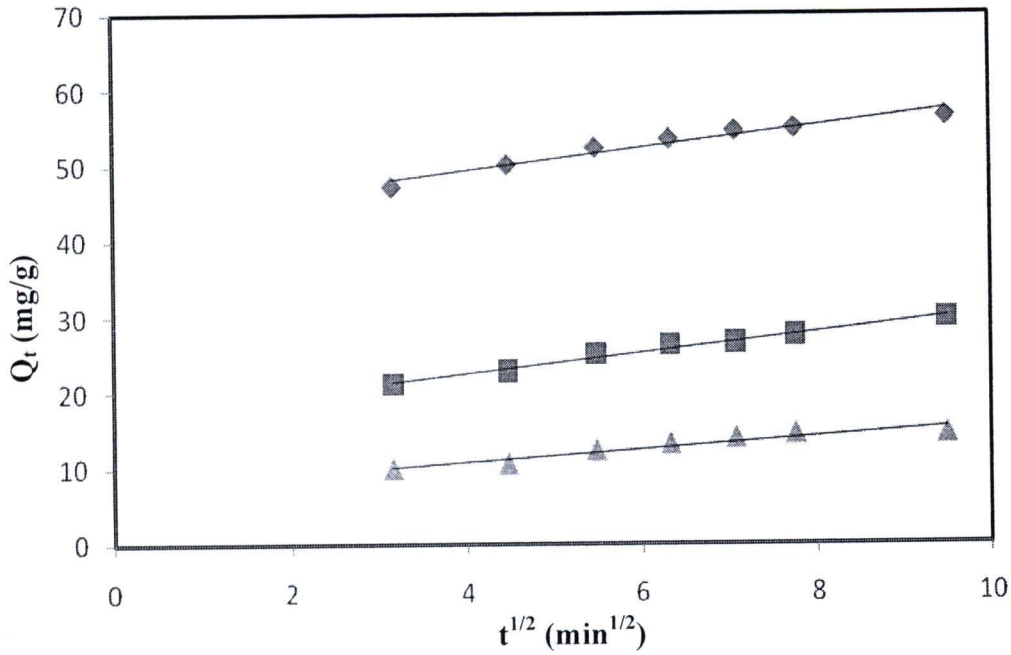

Figure 5.21 Regression of intraparticle diffusion model of (▲)MB, (♦)B5 and (■)R31:

For the intraparticle model, film diffusion was negligible and intraparticle diffusion was the only rate-controlling step. Although the regression of q versus $t^{1/2}$ within a range of time less than 60 minutes was linear as shown in figure 5.21, suggesting that the adsorption would partially relate with intra-particle diffusion.

5.5 Desorption and regeneration of exhausted CNPs

The condition of desorption experiment are initial dye concentration of 100 mg/l, 0.5 g/l adsorbent and 24 hours of adsorption time at 25 °C and the initial pH value of 6. All experiments use NaOH and HCl to adjust the pH solution. After adsorption, adsorbents were seperated from the solution by eternal magnetic and filter membrane (0.45 μm), and oven-dried at 80 °C to a constant mass. The solution was measured the concentration with UV-spectrophotometer.

Exhausted CNPs were suspended in distillated water which was adjusted the pH value for 5 hours for regeneration. In this study, the range of initial pH value of the solution is 3-11. Re-adsorption experiment following the procedure described above for 3 cycles. The desorption efficiency was calculated by the follow equation:

$$\text{Desorption efficiency (\%)} = \frac{Q_e - Q_d}{Q_e} \times 100$$

Where Q_e and Q_d are the equilibrium adsorbed amount and residual adsorbed amount of the dye after desorption, respectively.

Figure 5.22 represents the variation of desorption efficiency of dyes with varied pH. It was observed that desorption efficiency of B5 and R31 increased when increasing pH of solvent. It has been found that when pH increases from 3 to 11, desorption efficiency of both of dye increases from 21.51 to 33.93% and 26.08 to 45.26% for B5 and R31, respectively. It might be said that R31 can desorbed easily than B5 because R31 (Molecular weight = 864) are smaller than B5 (Molecular weight = 993). For MB desorption, although the size of MB is smallest (Molecular weight = 320) but the maximum desorption efficiency is 13.80% at pH value of solvent of 11. It should be noted that pH of solvent are not affect to desorbs MB.

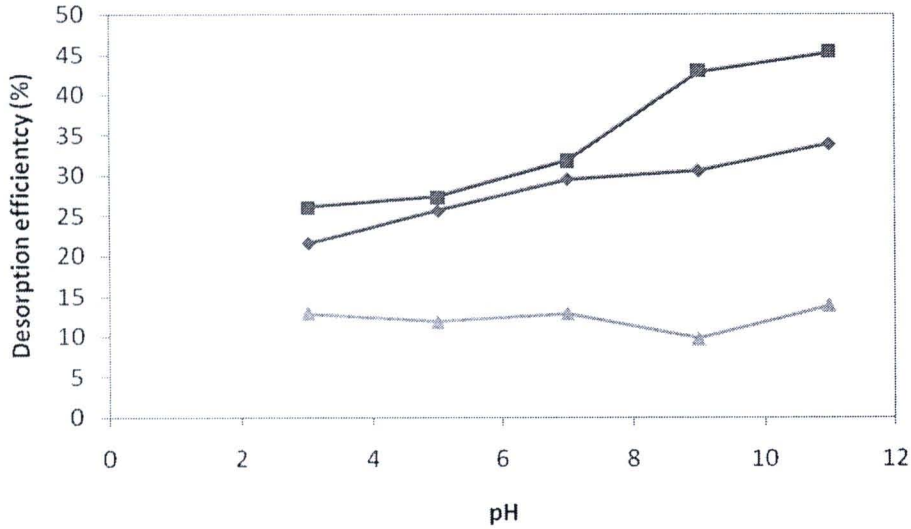

Figure 5.22 Effect of pH on desorption of exhausted CNPs

Over three adsorpton/desorption cycles, the re-adsorption efficiency result (as shown in Figure 5.23) was found that the loss in the sorption capacity between the first cycle and the last cycle was 33.07%, 48.99% and 19.97% for B5, R31 and MB, respectively.

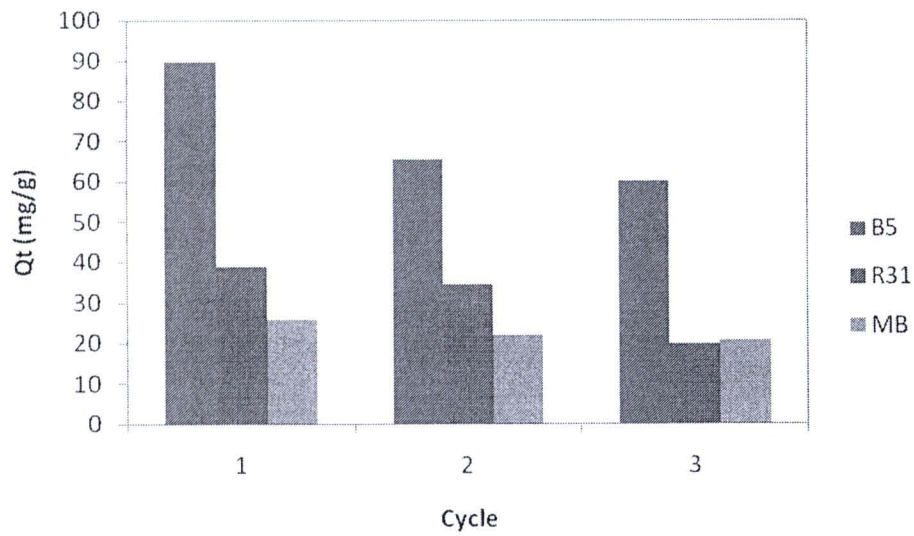

Figure 5.23 Sorption and re-adsorption of regenarate CNPs

5.6 Magnetic separation

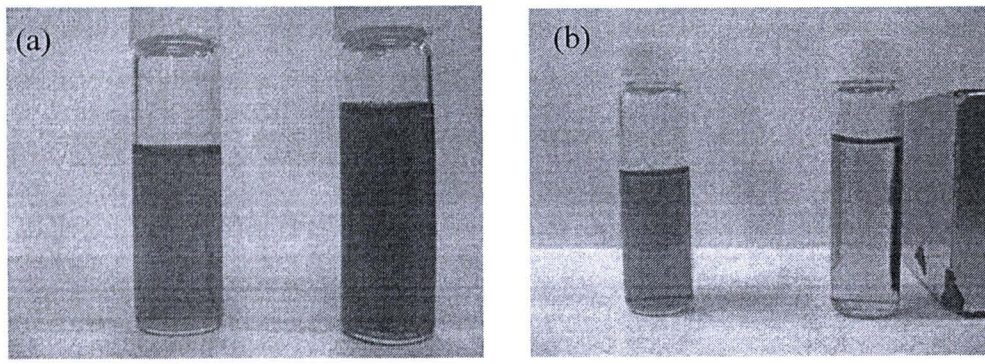

Figure 5.24 The magnetic separation: (a) suspension CNPs in aqueous dye solution and (b) CNPs attracted by external magnetic after adsorption process.

Figure 5.24 displays magnetic separation. In adsorption experiments, CNPs were suspended in aqueous solution as shown in figure 5.24 (a) for 5 h. After adsorption process, suspended CNPs were separated from the solution by external magnetic within 20 seconds as shown in figure 5.24 (b).

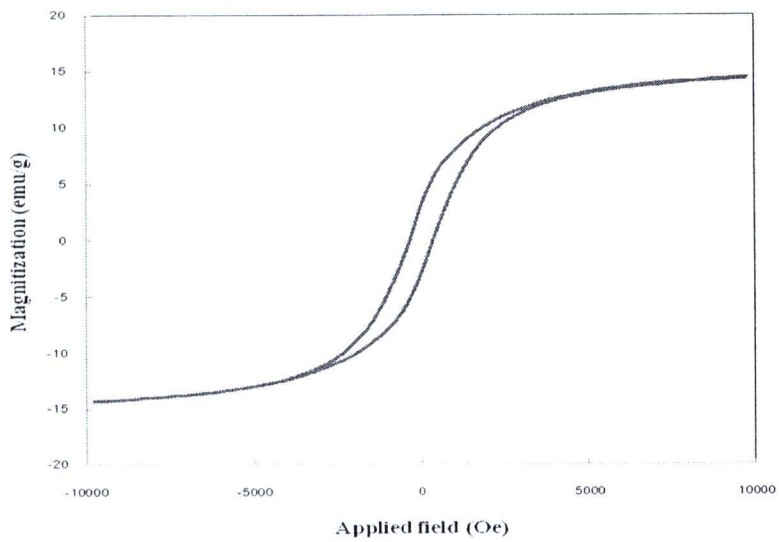

Figure 5.25 Magnetization curve of as-grown CNPs.

The hysteresis loop between ±10 kOe, which has a saturation magnetization of 14.25 emu/g (as shown in figure 5.25). The saturation magnetization of synthesized CNPs was higher than the other reported by Gong et al [16] and Zhu et al [20]. Based

on XRD results, the obtained CNPs showed the characteristic of ferromagnetism from bcc-Fe particles and superparamagnetism from fine Fe_2O_3 particles. The short time for CNPs separation from the solution after adsorption process exhibited high response rate with external magnetic field. Therefore, the synthesized CNPs are expected to be the novel solid adsorbent with the separation convenience process.